10884–10894 *Nucleic Acids Research, 2017, Vol. 45, No. 18* *Published online 5 September 2017*
doi: 10.1093/nar/gkx785

Structural insights into species-specific features of the ribosome from the human pathogen *Mycobacterium tuberculosis*

Kailu Yang[1], Jeng-Yih Chang[1], Zhicheng Cui[1], Xiaojun Li[1], Ran Meng[1], Lijun Duan[1], Jirapat Thongchol[1], Joanita Jakana[2], Christoph M. Huwe[3], James C. Sacchettini[1] and Junjie Zhang[1,*]

[1]Department of Biochemistry and Biophysics, Texas A&M University, College Station, TX 77843, USA, [2]National Center for Macromolecular Imaging, Verna and Marrs McLean Department of Biochemistry and Molecular Biology, Baylor College of Medicine, Houston, TX 77030, USA and [3]Bayer AG Pharmaceuticals, Global External Innovation & Alliances, 13342 Berlin, Germany

Received May 23, 2017; Revised August 17, 2017; Editorial Decision August 21, 2017; Accepted August 26, 2017

ABSTRACT

Ribosomes from *Mycobacterium tuberculosis* (*Mtb*) possess species-specific ribosomal RNA (rRNA) expansion segments and ribosomal proteins (rProtein). Here, we present the near-atomic structures of the *Mtb* 50S ribosomal subunit and the complete *Mtb* 70S ribosome, solved by cryo-electron microscopy. Upon joining of the large and small ribosomal subunits, a 100-nt long expansion segment of the *Mtb* 23S rRNA, named H54a or the 'handle', switches interactions from with rRNA helix H68 and rProtein uL2 to with rProtein bS6, forming a new intersubunit bridge 'B9'. In *Mtb* 70S, bridge B9 is mostly maintained, leading to correlated motions among the handle, the L1 stalk and the small subunit in the rotated and non-rotated states. Two new protein densities were discovered near the decoding center and the peptidyl transferase center, respectively. These results provide a structural basis for studying translation in *Mtb* as well as developing new tuberculosis drugs.

INTRODUCTION

Tuberculosis (TB) is a widespread infectious disease, affecting one third of the world's population and leading to ∼1.5 million annual deaths (http://www.who.int/tb/publications/global_report/en/). TB is caused by *Mycobacterium tuberculosis* (*Mtb*), whose success as a pathogen is dependent on its ability to persist within human hosts and resist antibiotics (1–4). During persistence, *Mtb* remains in a non-replicating state, minimizing most metabolic activities including translation (5). Genetic and biochemical studies have revealed that *Mtb* has incredibly sophisticated approaches to fine-tune translation, such as activating a dormancy survival regulator (DosR) regulon to control the ribosome stability in hypoxic mycobacteria (6,7), using toxin-antitoxin pairs to regulate the ribosome activity (8) or incorporating mistranslation to bypass inhibitors (9). It has also been shown that leaderless translation is common and robust in mycobacteria (10). These accumulating observations suggest the uniqueness of the mycobacteria translation system. However, the underlying mechanisms of these featured regulations in mycobacteria translation are not fully understood. We set out to solve high-resolution structures of the *Mtb* ribosome, a major drug target in TB (11), which will aid in understanding translational regulation in *Mtb* and serve as a structural framework to facilitate the rational design of new inhibitors.

Sequence analyses (12) have revealed that the *Mtb* ribosome contains species-specific structural features, such as extended or inserted rRNA helices, referred to as rRNA expansion segments (Figure 1A). It has recently been shown that, in yeast ribosomes, such rRNA expansion segments could be important for the appropriate assembly and function of the ribosome (13,14). However, structurally characterizing these large rRNA expansion segments remains challenging, mainly due to its presence on the peripheral of the ribosome, allowing large conformational variability. Compared with other, better studied bacterial ribosomes (15–18), the *Mtb* ribosome has a 100-nt rRNA expansion segment, referred to as H54a, or the 'handle', in its 23S rRNA. The structure and function of the handle has not been clearly defined.

Several *Mtb* rProteins are significantly longer than their counterparts in other model bacterial ribosomes, and there are several rProtein paralogs encoded by non-identical genes, which are differently expressed in response to varying physiological conditions (19). Moreover, the *Mtb* ribosome

*To whom correspondence should be addressed. Tel: +1 979 458 9882; Fax: +1 979 845 9274; Email: junjiez@tamu.edu

© The Author(s) 2017. Published by Oxford University Press on behalf of Nucleic Acids Research.
This is an Open Access article distributed under the terms of the Creative Commons Attribution License (http://creativecommons.org/licenses/by-nc/4.0/), which permits non-commercial re-use, distribution, and reproduction in any medium, provided the original work is properly cited. For commercial re-use, please contact journals.permissions@oup.com

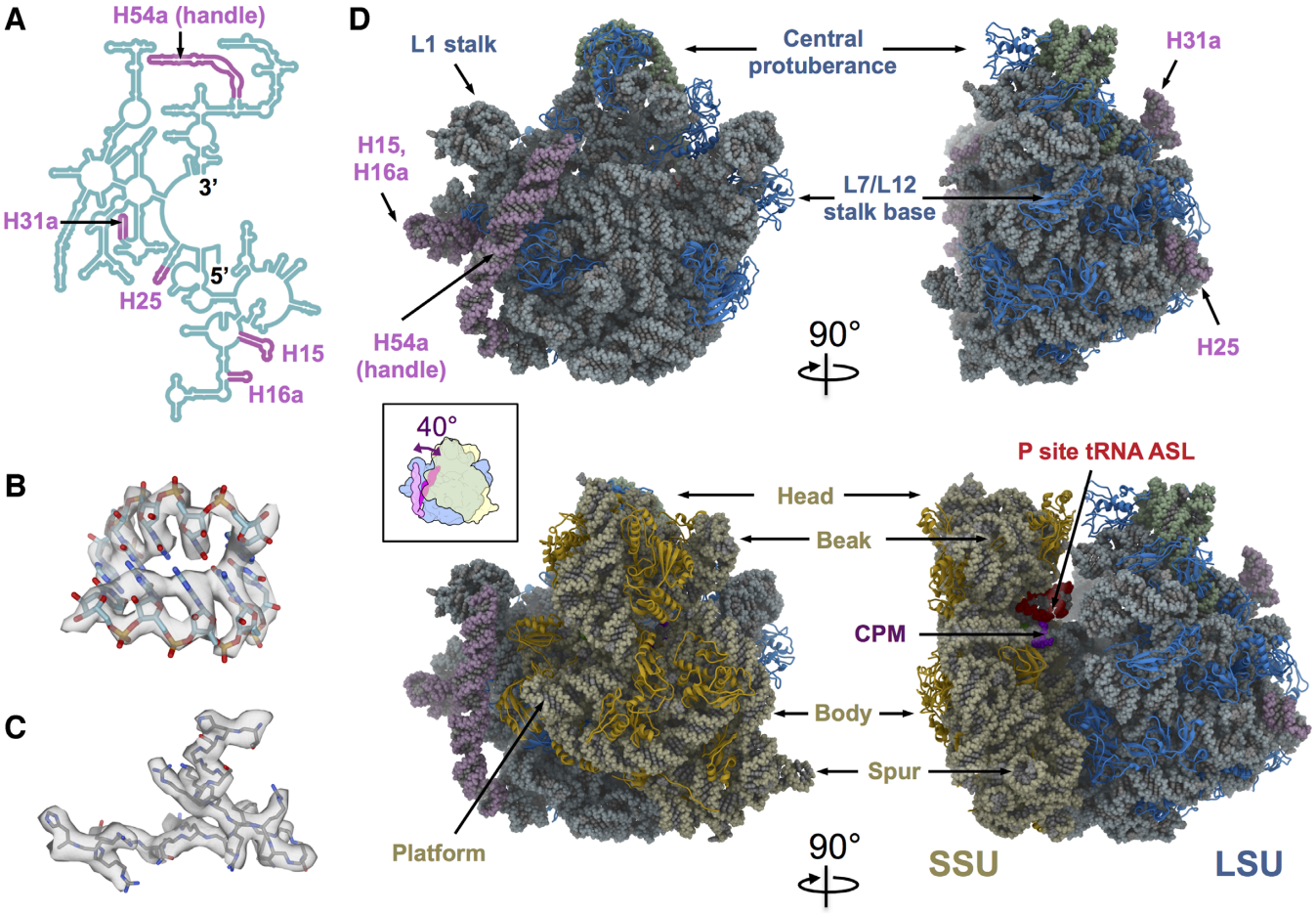

Figure 1. Cryo-EM structures of the *Mtb* 50S and 70S ribosomes. (**A**) Secondary structure of the 5′ half of the *Mtb* 23S, showing the positions of the *Mtb* expansion segments (plum color) within the 23S rRNA. (**B**) The model of a helix fragment of the 23S rRNA (residue 818–822 and residue 898–902) fits into the density from the *Mtb* 50S, showing individual RNA bases. (**C**) The model of bL35 (residues 6–31) fits into the density from the *Mtb* 70S, showing bulky protein side chains. (**D**) Overall structures of the *Mtb* 50S (top row) and 70S (bottom row) ribosomes viewing from the subunit interface (left column) and the L7/L12 stalk base (right column), respectively. Structural landmarks of the bacterial ribosome are labeled. Color schemes are dodger blue for LSU rProteins, light blue for 23S, plum for 23S rRNA expansion segments, green for 5S, gold for SSU rProteins, light yellow for 16S, purple for capreomycin (CPM) and red for the anticodon stem loop of the P-site tRNA. The cartoon in the inset box is an overlay of the 50S and 70S viewed from the SSU. The handle swings 40° counter-clockwise upon the association between SSU and LSU.

might have species-specific rProteins that have not been annotated based solely on sequence information. The three-dimensional (3D) structure of the *Mtb* ribosome will reveal these unique aspects of the *Mtb* ribosome to elucidate their roles in translation.

Here, we present the near-atomic cryo-electron microscopy (cryo-EM) structures of the *Mtb* 50S ribosomal subunit alone and the complete *Mtb* 70S ribosome, which reveal a dramatic conformational change of the handle. In addition, we observed correlated motions between the handle and other ribosomal components by comparing the conformational differences between various states of the *Mtb* 70S ribosome during spontaneous intersubunit rotation.

MATERIALS AND METHODS

Purification of *Mtb* and *Mycobacterium smegmatis* (*Msm*) ribosomes

Mtb and *Msm* ribosomes were purified as previously described (20). Briefly, MC^27000 *Mtb* or MC^2155 *Msm* cells were grown in 7H9 medium supplemented with 0.5% glycerol, 0.05% Tween-80 and OADC (BD) at 37°C until they reached an OD_{600} of around 1. All subsequent procedures were performed at 4°C. Harvested cells were lysed in a bead beater (BioSpec) in lysis buffer (20 mM Tris–HCl pH 7.5, 100 mM NH_4Cl, 10 mM $MgCl_2$, 0.5 mM EDTA, 6 mM β-mercaptoethanol). *Mtb* and *Msm* ribosomes were purified according to modified protocols. Cell lysates were clarified by centrifugation at 30 000 *g* for 1 h. The supernatant was pelleted in sucrose cushion buffer (20 mM HEPES pH 7.5, 1.1 M sucrose, 10 mM $MgCl_2$, 0.5 M KCl, and 0.5 mM EDTA) at 40 000 rpm in a Beckman Type 45Ti rotor for 20 h. The pellet was resuspended in a buffer containing 20 mM Tris–HCl pH 7.5, 1.5 M $(NH_4)_2SO_4$, 0.4 M KCl and 10 mM $MgCl_2$. The suspension was then applied to a hydrophobic interaction column (Toyopearl Butyl-650S) and eluted with a reverse ionic strength gradient from 1.5 M to 0 M $(NH_4)_2SO_4$ in a buffer containing 20 mM Tris–HCl pH 7.5, 0.4 M KCl, and 10 mM $MgCl_2$. The eluted ribosome peak was changed to either a reassociation buffer (5

mM HEPES-NaOH, pH 7.5, 10 mM NH_4Cl, 50 mM KCl, 10 mM $MgCl_2$ and 6 mM β-mercaptoethanol) or dissociation buffer (20 mM Tris–HCl, pH 7.5, 2 mM $MgCl_2$, 150 mM NH_4Cl, 50 mM KCl and 6 mM β-mercaptoethanol) then concentrated before applying to a 10–40% linear sucrose gradient centrifuged in a Beckman SW28 rotor at 19 000 *rpm* for 19 h. The 70S and 50S fractions were concentrated to about $A_{260} = 300$ after removal of the sucrose.

Cryo-electron microscopy

In total five samples were prepared for cryo-EM, including *Mtb* 50S with 10 mM Mg^{2+}, *Mtb* 50S with 1 mM Mg^{2+}, *Mtb* 70S with capreomycin, *Mtb* 70S without capreomycin and *Msm* 70S, for which the ribosome concentrations were diluted to 50 nM. *Mtb* 50S with 1 mM Mg^{2+} was diluted with the M1 dilution buffer (5 mM HEPES-Na, pH 7.5, 10 mM NH_4Cl, 50 mM KCl and 1 mM $MgCl_2$). The other samples were diluted with the M10 dilution buffer (5 mM HEPES-Na, pH 7.5, 10 mM NH_4Cl, 50 mM KCl and 10 mM $MgCl_2$). For *Mtb* 50S with 10 mM Mg^{2+}, 10 μM LZD-114 was added and then incubated for 30 min at 25°C. For *Mtb* 70S with capreomycin, 10 μM capreomycin was added and then incubated for 30 min at 25°C. A total of 3 μl of the sample was applied to a C-Flat 1.2/1.3 holey carbon grid, at 16°C with 100% relative humidity and vitrified using a Vitrobot Mark III (FEI company, The Netherlands).

The grids for *Mtb* 50S with 10 mM Mg^{2+} were imaged under a JEM-3200FSC transmission electron microscope operated at 300 KV. Data were recorded on a Gatan K2 Summit (Gatan, Pleasanton CA, USA) direct detection camera in the super-resolution electron counting mode. A nominal magnification of 40 000 × was used, yielding a pixel size of 0.82 Å on the specimen. The beam intensity is adjusted to a dose rate of 8 electrons per pixel per second on the camera. A 30-frame movie stack was recorded for each exposure of 6 s, at 0.2 s per frame.

The grids for *Mtb* 70S with capreomycin, and *Msm* 70S were imaged under an FEI Tecnai TF20 cryo electron microscope with a field emission gun (FEI company, The Netherlands) operated at 200 KV. Data were recorded on a Gatan K2 Summit (Gatan, Pleasanton CA, USA) direct detection camera in the super-resolution electron counting mode. A nominal magnification of 29 000 × yielded a pixel size of 1.25 Å on the specimen. The beam intensity was adjusted to a dose rate of 10 electrons per pixel per second on the camera. A 33-frame movie stack was recorded, with a 0.2 s exposure per frame. Additional data for *Mtb* 50S with 1 mM Mg^{2+} and *Mtb* 70S without capreomycin was collected using the similar procedure at a nominal magnification of 19 000 ×, yielding a pixel size of 1.87 Å on the specimen. All related information for data collection was summarized in Supplementary Table S1.

Image processing

The collected image stacks were aligned and summed using Unblur (21). The defocus value of each image stack was determined using CTFFIND4 (22). Good image stacks were selected based on the results from both programs. From the summed micrographs of the good image stacks, particles were semi-automatically picked using the *Erase* and *Swarm* tools of *e2boxer.py* in EMAN2 (23). The 2D and 3D classifications were performed in Relion1.4 (24) to get cleaner and more homogenous particles, then the particles were refined and polished (25) to get the final reconstructions. Overall resolutions were estimated according to the gold-standard Fourier shell correlation (26). Local resolutions were calculated using *blocres* from the Bsoft package (27). To further improve the map quality of the *Mtb* 70S small subunit (SSU), masked classification with signal subtraction (24) followed by masked refinement was performed in Relion1.4.

To examine the conformational dynamics of the handle, the *Mtb* 70S particles collected at 19 000 × magnification were merged with the dataset of *Mtb* 70S collected at 29 000 × magnification. Then the merged dataset was analyzed using masked classification with signal subtraction (24) followed by unmasked refinement of the entire *Mtb* 70S for each class in Relion1.4. Briefly, the particles were downscaled by a factor of 4 and refined into one consensus density map. Then a mask around the handle region was generated. The projections of the consensus map (except the handle region) were subtracted from the polished images using the orientation parameters from the consensus refinement, which generated new images of the handle alone. Then the new images were classified without alignment into 40 good classes, each of which was then refined to get a final reconstruction. We examined the particle distribution over different classes and found no significant difference between the two datasets of *Mtb* 70S with or without the capreomycin.

Molecular modeling

The following modeling procedures were performed first in the highest resolution maps, *i.e.* the large subunit (LSU) of the *Mtb* 50S and the locally refined SSU of the *Mtb* 70S. The sequences of *Mtb* 5S, 16S and 23S rRNA were obtained through NCBI Gene with the Gene ID 2700459, 2700429 and 2700466, respectively. Template-based comparative modeling was performed using modeRNA (28). The *Escherichia coli* 70S structure (PDB ID: 5AFI) (16) was chosen as the template. The sequence alignment of rRNA in bacteria was downloaded from the comparative RNA website (CRW) (12). The rRNA expansion segments were manually built in Assemble2 (29) with the aid of the secondary structures that were constructed based on the downloaded sequence alignment, and then refined into the density map using MDFF (30). The rRNA was refined in PHENIX (31), with restrictions of secondary structures. ERRASER (32) was also used to improve the RNA backbone geometry. The sequences of *Mtb* rProteins were obtained from the NCBI database. MODELLER (33) was used to generate the initial homology models. Rosetta (34) was used to refine the homology model of each rProtein into the density map. The best model was selected from the Rosetta refinement based on both the geometry and the fitting scores. The rRNA and rProtein models were merged into one model and subsequently refined using Rosetta and PHENIX. During the above modeling process, Coot (35) was iteratively used to inspect and improve the local fitting.

To obtain a full model of the *Mtb* 70S ribosome, the models of the *Mtb* 50S and 30S from the above procedures were

merged together with adjustment of the interface between the two subunits. For the handle in the *Mtb* 70S, we used MOSAICS-EM (36) to flexibly fit the handle into the density of the dominant conformation, while ensuring its connectivity to the other part of the LSU. The 70S map has low local resolutions in some certain regions, including the tip of the handle and the periphery of the SSU. To prevent any improper refinement of high quality models into these poor quality regions, we added the density of the dominant handle conformation and the density of the locally refined SSU to the 70S map to refine the entire 70S model. Both models of the *Mtb* 50S and 70S were inspected and adjusted in Coot, and iteratively refined in Rosetta and PHENIX. The statistics, obtained by using PHENIX and MolProbity (37), of the refined models are listed in Supplementary Table S2.

Fitting the models for the 40 conformations of the L1 stalk, the handle and the 16S

The Hierarchical Natural Move Monte Carlo or HNMMC as implemented in MOSAICS-EM (36) was applied to refine the handle and the L1 stalk into all 40 obtained EM density maps. The HNMMC allows the user to group atoms into regions with collective motions (38) to increase the efficiency of conformational sampling. For the 40 conformations of the 16S, we first segmented out the densities for 16S only and then used MOSAICS-EM to refine the 16S model into its density.

Principal component analysis of the *Mtb* 70S structures

The principal component analysis was performed on 40 models of the handle, the L1 stalk, and the 16S rRNA using the Bio3D package (39). Only the C4' atoms were used in calculating the principal components.

Figures and movies preparation

All figures and movies were made using UCSF Chimera (40) and XRNA (http://rna.ucsc.edu/rnacenter/xrna/).

RESULTS AND DISCUSSION

Architecture of the *Mtb* ribosomes

The *Mtb* 70S ribosome consists of an LSU (or 50S) and an SSU (or 30S). For consistency throughout the text, we will use 50S and 70S to refer to the two ribosome specimens and use LSU and SSU to refer to the two ribosomal subunits. For example, the *Mtb* 50S specimen contains only the LSU while the *Mtb* 70S specimen contains both the LSU and SSU. The *Mtb* LSU is composed of rRNA 23S, rRNA 5S and about thirty rProteins, while the *Mtb* SSU is made of rRNA 16S and about 20 rProteins.

Using single-particle cryo-EM, structures of the purified *Mtb* 50S ribosomal subunit and 70S ribosome were determined to overall resolutions of 3.7 Å and 4.0 Å, respectively (Supplementary Table S1 and Figure S1). Cryo-EM densities in the core region of the *Mtb* ribosomes showed clear features of individual RNA bases (Figure 1B) as well as the bulky side chains of the rProteins (Figure 1C). In the cryo-EM map of the *Mtb* 70S, the SSU exhibited a large degree of flexibility, leading to a lower local resolution. To improve the quality of the structure, densities of the SSU were extracted from the particle images for the entire *Mtb* 70S (24) and processed separately. This approach allowed us to resolve the SSU to an overall resolution of 4.5 Å (Supplementary Figure S1). The models of *Mtb* 50S and 70S were built (see 'Materials and Methods' section) and the model statistics are summarized in Supplementary Table S2.

The resultant structures of the *Mtb* 50S and 70S ribosomes showed that the overall architecture is conserved compared with other bacterial ribosomes, possessing all the structural landmarks, including the central protuberance, the L1 stalk and the L7/L12 stalk base of the LSU, as well as the head, the beak, the body, the spur and the platform of the SSU (Figure 1D). In the *Mtb* 70S structure, the density for the anticodon stem loop of the P-site tRNA, along with the mRNA, is clearly visible, showing base pairing between the codon and the anticodon (Supplementary Figure S2). We have resolved most of the rProteins and modeled them into the density with the exception of rProteins uL1, uL10, uL11, bL12, bS1 and uS2, due to the flexibility or absence of these proteins in our structure (Supplementary Table S3).

The secondary structures of all the *Mtb* rRNAs 23S, 16S and 5S, were built based primarily on sequence alignment (12) (Supplementary Figure S3). All the rRNA expansion segments in the *Mtb* ribosomal LSU are located in the 5′ half of the rRNA 23S (Figure 1A) and have all been identified in our *Mtb* ribosomal structures (Figure 1D). Expansion segments for H25 and H31a are located on the solvent exposed side of the LSU, away from the SSU, with H25 leaning toward the L7/L12 stalk base and H31a leaning toward the central protuberance. Expansion segments H15 and H16a are located on the solvent exposed side of the LSU, close to the L1 stalk, with their tips forming an RNA kissing loop (Supplementary Figure S4a). From the CRW (12), we have identified expansion segments of H15 and H16a in the 23S from eight different bacteria (*M. tuberculosis, Mycobacterium leprae, Micrococcus luteus, Streptomyces ambofaciens, Thermotoga maritima, Leptospira interrogans, Borrelia burgdorferi* and *Treponema pallidum*). Seven of the eight bacterial species have nucleotide bases at the tips of the H15 and H16a supporting Watson-Crick base pairing to form a kissing loop (Supplementary Figure S4b). The only exception is *T. pallidum*, whose H15 is about 20 nt shorter than the H15 in the other seven bacteria, and is therefore unable to form a kissing loop with H16a. The rRNA expansion segment of H15 from the *Mtb* ribosome interacts directly with the long α-helix of rProtein bL9, which connects the two globular domains at the N-terminal and C-terminal ends. This extended H15, stabilized by the kissing loop between H15 and H16a, may provide an additional structural anchor for binding the long connecting α-helix of bL9 (Supplementary Figure S5).

The cryo-EM density for the 100-nt long rRNA expansion segment, handle, is well defined in the *Mtb* 50S density map. However, in the 70S map, density for the tip of the handle is missing, suggesting significant levels of conformational variability among the handles in the 70S particles. To better resolve the structures of the handle in *Mtb* 70S, an unsupervised classification was performed locally on the handle to generate 40 maps of the *Mtb* 70S ribosome, each

showing more complete density of the handle in that particular conformation (Supplementary Figure S6). The resolutions of these 40 maps of the *Mtb* 70S range between 6.6 Å and 12.8 Å (Supplementary Table S4). Five representative conformations of the handle in *Mtb* 70S are shown in Supplementary Figure S7. The dominant conformation is conformation I, where the ribosome is in the non-rotated state and the handle is closer to the L1 stalk. In conformations I, II and III, the densities of the handle and the bS6 are connected, while in conformations IV and V, they are disconnected.

The better densities of the handles obtained for the 40 classes of the *Mtb* 70S, allowed us to compare it with its corresponding density in the *Mtb* 50S. The handle showed a remarkable conformational change between the *Mtb* 50S and the *Mtb* 70S structures. In the 50S, the handle is bent toward the central protuberance; the dominant conformation of the 70S shows the handle tilted toward the L1 stalk. The handle moves about 40° from its primary orientation in the 50S to the predominant conformation in the 70S. This movement effectively translates into the tip traveling about 60 Å from one state to the other (inset of Figure 1D).

Interactions between handle and other regions in the *Mtb* ribosome

In the *Mtb* 50S structure, three loops on the solvent exposed side of uL2 (amino acid residues 168–170, 134–136, 121–123; labeled with blue stars from top to bottom in Figure 2A) form interactions with a minor groove on the handle (nucleotide residues 1576–1580 and 1626–1630). There is another interaction (labeled by a black star in Figure 2A) between residue 1591A of the handle and a minor groove of helix H68 of the 23S (formed by nucleotides 2079–2081 and 2132–2134). The interactions of the handle with H68 (Figure 2C) and uL2 (Figure 2D) appear to be stable within the *Mtb* 50S structure and not an artifact of a high magnesium concentration (41), as reducing the magnesium concentration in the buffer to 1 mM does not affect these interactions (Supplementary Figure S8). Interestingly, in the *Mtb* 70S model, the same minor groove of helix H68 interacts with an unpaired adenine (nucleotide residue 693A) on the 16S rRNA of the SSU, forming intersubunit bridge B7a.

In bacterial ribosomes, rProtein uL2 interacts with rRNA in the SSU to form the intersubunit bridge B7b (42). When we directly superimposed the 50S structure onto the *Mtb* 70S, the handle in the *Mtb* 50S specimen collides with both rProtein uS11 and helix h23 of the 16S rRNA in the 70S (Supplementary Movie S1). Thus, the conformation of the handle seen in the 50S would not allow the direct association of the SSU with the LSU. Moreover, if the handle remained in the same conformation as in the 50S, the tip of the handle would be in close proximity to the initiator tRNA in the initiation complex (Supplementary Figure S9) (43). This position suggests the handle may play a role in coordinating translation initiation in the *Mtb* ribosome, such as the handle staying in this bent conformation in the *Mtb* 50S to prevent the association of the 30S until the initiation complex is properly formed.

The 70S structure shows that when the subunits associate to form the mature 70S, the handle forms a new intersubunit bridge with rProtein bS6 (named B9, Figure 2B and E). Bridge B9 (labeled with an orange star in Figure 2B) comprises interactions between an α-helix from rProtein bS6 (amino acid residues 12–17) and the minor groove of the handle (residues 1576–1578 and 1628–1630). About 80% of the *Mtb* 70S particles have the B9 bridge maintained (Supplementary Table S4).

In the most dominant conformation, the handle also interacts with rProtein bL9 (Figure 2B and E) with the C-terminal domain of bL9 inserted into a major groove of the handle (nucleotide residues 1571–1573 and 1625–1626, Figure 2F). In a recent high-resolution cryo-EM structure of the *E. coli* ribosome, *E. coli* bL9 was shown to interact with both uL2 and bS6 (16). However, in the *Mtb* 70S ribosome, the handle can interact with the C-terminal domain of bL9 and may serve as a substitution for the interaction between bL9 and bS6 (Figure 2E). rProtein bL9 is highly flexible in the ribosome and has been shown to be involved in mRNA bypassing during the translation of the T4 phage gene 60 (44). Gene disruption of bL9 in *E. coli* increases the translational error rate when the cell is under stress, e.g. being treated with antibiotics (45). These observations, in combination with structural information from ribosomes and polysomes, led to the proposal that bL9 may slow the forward movement of ribosomes that trail transiently stalled ribosomes on the polysome. However, in *Mtb*, the extended RNA helices and the handle may further restrain the flexibility of bL9.

In particular, the handle contains a GAA-AGUA sequence (labeled red in Figure 2F), located at the bottom of this long RNA helix, to form a sarcin-ricin motif (or bulged-G motif) (46). The sarcin-ricin motif serves as a recognition site for RNAs and proteins (47,48), which may aid in target binding (49). Of note, many toxins, including α-sarcin (50), ricin A-chain (51), Shiga toxin (52) and VapC20 (53), bind to the sarcin-ricin motif in the sarcin-ricin loop (54) and cleave the nearby rRNA. The sarcin-ricin motif in the handle is exposed to solvent, as in the sarcin-ricin loop, thus accessible to its potential binding partners. It is yet to be discovered that such binding partners do exist or that a cleavage can occur in the *Mtb* handle, which may serve as a 'switch' to control the potential translational modulation by the handle.

Correlated motions of the handle, the L1 and the SSU in the *Mtb* 70S

The *Mtb* 70S exhibits significant structural variation among the 40 different density maps calculated from the 3D classification (see 'Materials and Methods' section, Supplementary Figure S6), each representing a snapshot between the rotated and the non-rotated states of the *Mtb* 70S ribosome (Figure 3A) during the spontaneous intersubunit rotation (55). Analysis of these states shows that the majority of the LSU remains unchanged. From the rotated to the non-rotated *Mtb* 70S with the LSU aligned, the SSU rotates clockwise when viewed from its solvent exposed side; the L1 stalk moves away from the tRNA binding sites and the handle moves toward the L1 stalk (Figure 3B and C; Supplementary Movie S2). To further delineate motions in the *Mtb* 70S, we built structural models for each of the 40

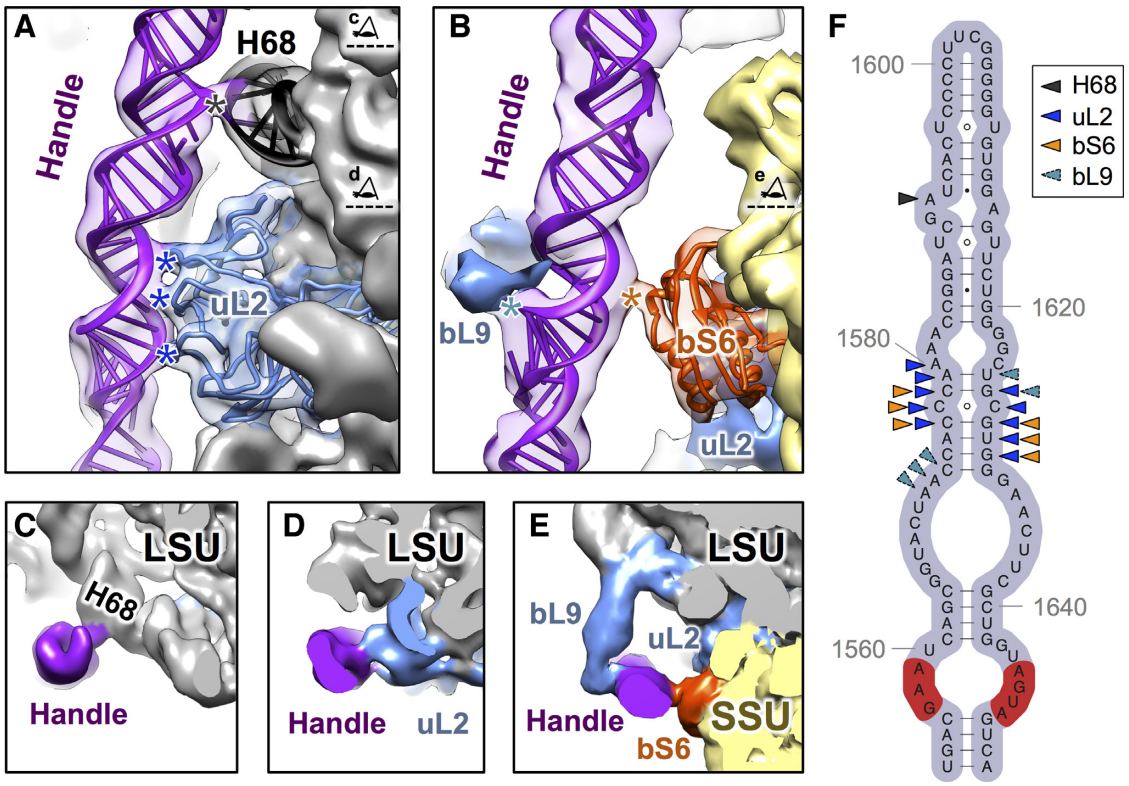

Figure 2. Interactions of the handle with other ribosomal components within the *Mtb* ribosomes. (**A**) Ribbon models showing where the handle (purple) interacts with rProtein uL2 (blue) and H68 (black) when in the 50S alone. The cryo-EM density of the 50S is low-pass filtered to 8Å resolution and overlaid onto the model. Black and blue stars indicate the sites of interactions from the handle to H68 and uL2, respectively. The two eye cartoons, top and bottom, label the cutting plane and viewing direction for Panels **C** and **D**, respectively. (**B**) Ribbon models show the handle interacts with bS6 (orange red) in the 70S. The cryo-EM density for the predominant conformation of the 70S is low-pass filtered to 8Å resolution and overlaid onto the model. Densities of rProteins bL9 and uL2 are colored blue. Cyan and orange stars indicate the sites of interactions from the handle to bL9 and bS6, respectively. The eye cartoon labels the cutting plane and viewing direction of Panel **E**. (C–E) Cryo-EM densities showing the handle interact with H68, uL2, bS6 and bL9. The 50S is labeled grey with uL2 and bL9 in blue while the handle is in purple. The 30S is in yellow with the rProtein bS6 in orange red. (**F**) Secondary structure of the handle with arrow heads indicating the nucleotides that interact with H68 (black), uL2 (blue), bS6 (orange) and bL9 (cyan). The sequence, which can form the sarcin-ricin motif, is colored in the red background.

snapshots of the SSU, the L1 stalk and the handle. Then we subjected them to principal component analysis, which revealed their dominant modes of motion (39). The first principal components of the motions for the SSU (represented by the rRNA 16S), the L1 stalk, and the handle, are the rotation of the SSU relative to the LSU, the tilt of the L1 stalk, and a large conformational change of the handle between the mRNA exit and the L1 stalk. (Supplementary Figure S10a and Movie S3). Each principal component 1 (PC1) represents 93, 82 and 68% of their total motions for the SSU, the L1 stalk and the handle, respectively. Therefore, each PC1 approximates their dominant structural variations. Projecting the 40 conformations of the SSU and the L1 stalk onto their respective PC1s clearly shows a correlation between the major movements of the SSU and the L1 stalk (Supplementary Figure S10b), which is consistent with the previous finding that the movement of the L1 stalk is directly linked to the rotation of the SSU (56). Remarkably, in most of the *Mtb* 70S conformations, the major motion of the handle exhibits a strong correlation with the major movements of both the L1 stalk and the SSU (Supplementary Figure S10c and d). When the SSU rotates clockwise and the L1 stalk moves away from the E-site, the handle moves close to the L1 stalk and *vice versa*. These concerted movements are consistent with a simple morphing between the rotated and non-rotated conformations of the *Mtb* 70S in Figure 3. Only about 20% of the *Mtb* 70S particles do not show such correlation of the handle to either the SSU or the L1 stalk. Closer inspection revealed that these 20% of the particles are missing the B9 bridge, resulting in less restrained movement of the handle.

The large conformational changes of the handle, which are correlated with the movement of the L1 stalk and SSU, may affect the translocation of the *Mtb* ribosome. For example, as the tRNA translocates between different sites on the ribosome, the SSU rotates and the L1 moves. As the handle moves around the exit sites of the mRNA and tRNA, it may coordinate the exit of the tRNA and the mRNA. Inspection of the different states of the *Mtb* 70S revealed that the tip of the handle is close to the mRNA exiting site in several rotated states. In fact it is <20 Å from the anti-Shine-Dalgarno sequence on the rRNA 16S in several conformations (Supplementary Figure S11). The anti-Shine-Dalgarno sequence has been shown to drive translational pausing and codon choice in bacteria (57), and the

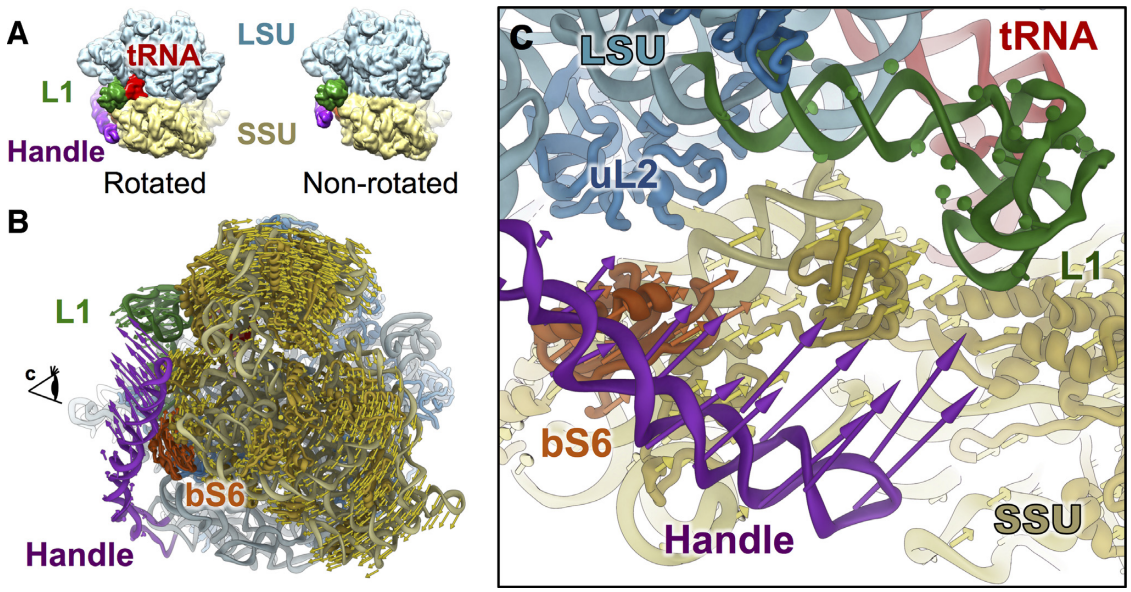

Figure 3. Correlated motions between the handle, SSU and the L1 stalk in the *Mtb* 70S ribosome. (**A**) *Mtb* 70S in the rotated (left) and non-rotated (right) states. (**B**) Conformational difference between the rotated and non-rotated states of the *Mtb* 70S viewing from the solvent exposed side of the SSU. The SSU, L1 stalk, handle and bS6 on the SSU are colored yellow, green, purple and orange red, respectively. Colored arrows indicate the directions and amplitudes of the conformational differences for the handle (purple), the L1 stalk (green), the SSU (yellow) and the bS6 (orange red) on the SSU. (**C**) Zoom-in view around the handle as viewed from the direction indicated by the eye cartoon in Panel B.

close proximity of the handle to this region of the *Mtb* ribosome may well affect *Mtb* translation.

Interestingly, in eukaryotic ribosomes, there is an rRNA expansion segment ES27, which undergoes conformational changes upon the rotation of the ribosomal subunits (58), similar to what have been observed for the handle of the *Mtb* ribosome. ES27 has been proposed to perform essential functions (59), such as coordinating non-ribosomal factors or interfering with the nascent peptide around the peptide exit tunnel. The handle in *Mtb* may reach the exiting tRNA and mRNA and its potential functions are still under investigation. Future cryo-EM studies of the *Mtb* polysome may reveal potential interactions between these structural components.

Inhibitors visualized in the *Mtb* ribosome

The potent ribosomal inhibitors capreomycin and LZD-114 (a linezolid analog, Supplementary Figure S12) were pre-incubated with the *Mtb* 70S and the *Mtb* 50S, respectively, prior to cryo-EM sample preparation. Capreomycin binds to the conserved decoding center, which is near helix h44 of the 16S (Figure 4A and B), in agreement with a crystal structure of capreomycin bound to the *Thermus thermophilus* ribosome (60).

LZD-114 is about 20 times more potent against the *Mtb* ribosome than linezolid (the IC_{50} of LZD-114 is 0.7 μM; the IC_{50} of linezolid is 14 μM; Supplementary Figure S12). The density of LZD-114 was observed in the peptidyl transferase center (PTC) of the *Mtb* 50S ribosomal subunit. It is bound in the same pocket and in a similar orientation to linezolid in other bacterial ribosomes (18,61,62). The improved potency of the LZD-114 may be due to the lack of a fluorine group in the B-ring and the substitution of the morpholine ring with a thiazole ring. The thiazole group is in close proximity to rRNA to form potential hydrogen bonds, *i.e.* the sulfur in the thiazole ring and the O2′ of the U2744. Linezolid is not desirable as a TB treatment, for an off-target inhibition of the human mitochondrial ribosome (mitoribosome) (63,64). A superimposition of the *Mtb* 70S and the human mitoribosome (Supplementary Figure S13) (65) showed that the binding site of LZD-114 is highly conserved, with only three residues difference between the two ribosomes within 10 Å of the LZD-114 binding site, namely A2296, C2745 and C2848 in the *Mtb* ribosome and G2721, U2994 and U3097 in the human mitoribosome. While the positions and orientations of these three nucleotide bases in the *Mtb* ribosome and the human mitoribosome are nearly identical, differences do exist, with one oxygen atom for each of the three bases (O6 in G2721, O4 in U2994 and U3097) of the human mitoribosome being replaced by a nitrogen atom (N6 in A2296, N4 in C2745 and C2848) in the *Mtb* ribosome, respectively. These small differences in the drug-binding pocket may be used to optimize linezolid analogs to avoid the off-target inhibition of the human mitoribosome.

Two new protein densities close to the functional sites of the *Mtb* ribosome

In the cryo-EM maps of the *Mtb* ribosomes, we observed densities for two distinct unknown proteins with clear α-helical geometries. One was positioned close to the decoding center where capreomycin binds, and the other close to the PTC near the LZD-114 binding site. Neither of these proteins has been observed in previously solved bacterial ribosome structures. Based on the full length and modeled

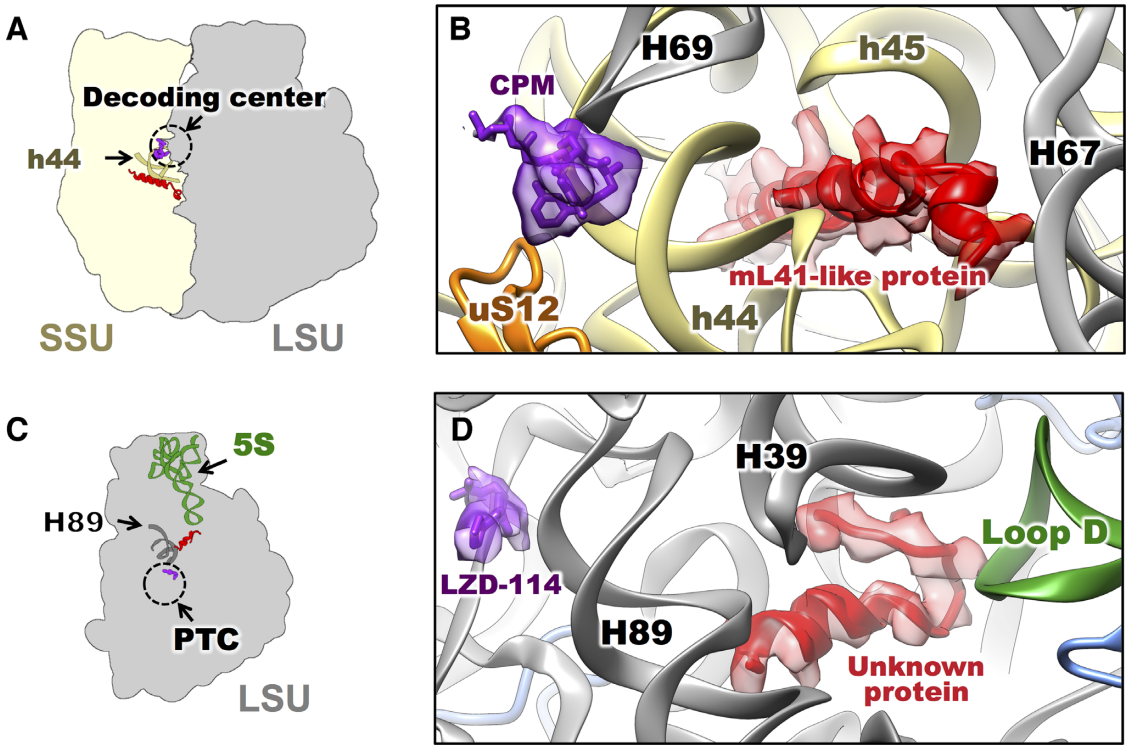

Figure 4. Unidentified proteins in the Mtb ribosomes discovered near the binding sites for two Mtb translation inhibitors. (**A**) Cartoon indicating the locations of the mL41-like protein (red), the antibiotic capreomycin (CPM, purple) in the structure of *Mtb* 70S incubated with capreomycin. Helix h44 of the 16S is in dark yellow. The dashed circle indicates the decoding center. (**B**) Zoom-in view to show the models of CPM (purple) and polyalanine model of the mL41-like protein (red) and their neighboring environment. SSU protein uS12 (orange), helices h44, h45 of the 16S (yellow) and helices H67, H69 of the 23S (grey) are labeled. (**C**) Cartoon indicating the locations of the unknown protein (red), the linezolid analog 114 (LZD-114, purple) in the structure of *Mtb* 50S incubated with LZD-114. The 5S is in green. The H89 is in dark gray. The dashed circle indicates the PTC. (**D**) Zoom-in view to show the models of LZD-114 (purple) and polyalanine model of the unknown protein (red) and their neighboring environment. H39, H89 of the 23S (gray) and Loop D of the 5S (green) are labeled.

sequences of nearby rProteins, these new structures do not correspond to any extensions of nearby rProteins.

The first protein, located close to the decoding center, is estimated, based on the density, to be about 30 amino acids long (Figure 4A and B). Interestingly, it has a very similar fold and is in the same location as that of eL41 and mL41, the rProteins found in eukaryotic cytosolic ribosomes and mitoribosomes, respectively (Supplementary Figure S14a–f). The protein lies in a pocket formed by h44 and h45 from the 16S on the SSU and H67 and H69 from the 23S on the LSU, near the pivot point of intersubunit rotation (66). This pocket is highly conserved in ribosomes across species (12,15,65–69). While *E. coli* and other bacterial ribosomes have this pocket empty (16), the ribosomes from *Saccharomyces cerevisiae*, *Homo sapiens*, *S. cerevisiae* mitochondria and *H. sapiens* mitochondria all show an α-helical protein in this pocket (65,66,69,70), which overlaps with this 'mL41-like protein' from *Mtb* (Supplementary Figure S14).

The second protein, close to the PTC, has not been identified in any bacterial, archaeal, yeast or mammalian ribosome structures. It is an α-helix and coil loop that sits in a chamber formed by H39 and H89 of the 23S rRNA, and the loop D of the 5S rRNA. Building a polyalanine model into the density allowed us to estimate the unknown protein to be around 20 amino acids long. Related density is also observed in the 7.1 Å resolution cryo-EM structure of the ribosome from *Mycobacterium smegmatis* (*Msm*, Supplementary Figure S15). The pocket formed between H39 and H89 of rRNA 23S, and loop D of rRNA 5S is very similar among the 70S ribosomes from bacteria and chloroplasts. In the *E. coli* ribosome this pocket is empty, but both the *Mtb* and chloroplast ribosomes have a protein in this pocket (Supplementary Figure S13g–i), that interacts with the loop D of rRNA 5S.

It has been proposed that the 5S rRNA is uniquely positioned to link all the functional centers of the ribosome. Previous studies have supported the hypothesis that the 5S acts as a physical transducer of information, facilitating communication between the different functional centers and coordinating multiple events catalyzed by the ribosome (71). By interacting with loop D of the 5S, an rProtein in this location may stabilize the interactions between H38, H89 and the loop D of the 5S. The name of the corresponding protein in chloroplast ribosomes is cL38 (72) or PSRP6 (73,74). The identity of this protein in *Mtb* is yet to be determined, but its orientation and length in the *Mtb* ribosome is different from cL38 (72–74). Notably, one end of the helix of this protein is close to H89, a major component of the PTC.

In summary, we have shown the *Mtb* ribosome has several species-specific features, including the handle and two new proteins. In the *Mtb* 50S, the handle stays in a bent conformation, which blocks the association of the SSU. From

the 50S to the 70S, the handle undergoes a large-scale conformational change to form intersubunit bridge B9. In the *Mtb* 70S, the handle shuttles between the L1 and the mRNA exiting site, which correlates with the rotation of the SSU.

While our manuscript was in review, a cryo-EM structure of the *Msm* 70S ribosome was reported (75). Despite the great interest of the unique handle conformation in 50S ribosomal subunit, the *Msm* 50S structure was not reported. Therefore, only the comparison of the 70S structures is possible. In the conserved core region, the *Mtb* 70S structure is in good agreement with the *Msm* 70S structure. However, in the peripheral region where most of the species-specific features exist, the *Mtb* 70S shows interesting difference from the *Msm* 70S structure. For example, the *Msm* paper reported an 'altered' conformation of bL9, which was proposed as one possible effect of the kissing loop between H15 and H16a. However, such a conformation of bL9 in *Msm* may not be universal in mycobacteria, particularly in the human pathogen, *Mtb*. In our *Mtb* ribosome structure, the bL9 mainly exhibits a different conformation, which directly interact with the handle, even in the presence of a similar kissing loop (Figure 2). The fact that the same protein bL9 has distinct conformations in *Mtb* and *Msm*, further emphasizes the necessity and clinical relevance of performing structural studies using the exact pathogen, with respect to a closely related non-pathogenic model organism.

DATA AVAILABILITY

Cryo-EM density maps have been deposited in the Electron Microscopy Data Bank under the accession numbers EMD-8641, 8645, 8646, 8647, 8648 and 8649 for *Mtb* 50S with LZD-114, *Mtb* 70S with capreomycin, the *Mtb* locally refined SSU, *Msm* 70S, the 40 *Mtb* 70S conformations (as one entry) and *Mtb* 50S with 1 mM Mg^{2+}, respectively. The atomic models of the *Mtb* 50S and 70S ribosomes have been deposited in the Protein Data Bank under the accession number 5V7Q and 5V93, respectively. Other data that support the findings of this study are available from the corresponding author upon request.

SUPPLEMENTARY DATA

Supplementary Data are available at NAR Online.

ACKNOWLEDGEMENTS

We acknowledge the Texas A&M High Performance Research Computing Center for providing the computational resources for the data processing. We thank Karl Gorzelnik and Tracey Musa for comments and editing of the paper. We thank Rhiju Das for the insightful discussion of the sarcin-ricin motif in the handle. We acknowledge the Microscopy and Imaging Center at Texas A&M University and the National Center for Macromolecular Imaging (NCMI) at Baylor College of Medicine for cryo-EM data collection.

FUNDING

Welch Foundation Grants [A-1863, A-0015]; National Institutes of Health TB Structural Genomics Grant [P01AI095208]; National Institutes of Health Grants [P41GM103832, U24GM116787]; Department of Biochemistry and Biophysics Start-up Fund (to J.Z.); Center for Phage Technology at Texas A&M University Start-up Fund (to J.Z.). Funding for open access charge: Welch Foundation Grant [A-1863].
Conflict of interest statement. None declared.

REFERENCES

1. Flynn,J.L. and Chan,J. (2001) Tuberculosis: latency and reactivation. *Infect. Immun.*, **69**, 4195–4201.
2. Wayne,L.G. and Sohaskey,C.D. (2001) Nonreplicating persistence of mycobacterium tuberculosis. *Annu. Rev. Microbiol.*, **55**, 139–163.
3. Smith,C.V., Sharma,V. and Sacchettini,J.C. (2004) TB drug discovery: addressing issues of persistence and resistance. *Tuberculosis (Edinb)*, **84**, 45–55.
4. Trauner,A., Borrell,S., Reither,K. and Gagneux,S. (2014) Evolution of drug resistance in tuberculosis: recent progress and implications for diagnosis and therapy. *Drugs*, **74**, 1063–1072.
5. Chao,M.C. and Rubin,E.J. (2010) Letting sleeping dos lie: does dormancy play a role in tuberculosis? *Annu. Rev. Microbiol.*, **64**, 293–311.
6. Kumar,A., Majid,M., Kunisch,R., Rani,P.S., Qureshi,I.A., Lewin,A., Hasnain,S.E. and Ahmed,N. (2012) Mycobacterium tuberculosis DosR regulon gene Rv0079 encodes a putative, 'dormancy associated translation inhibitor (DATIN)'. *PLoS One*, **7**, e38709.
7. Trauner,A., Lougheed,K.E., Bennett,M.H., Hingley-Wilson,S.M. and Williams,H.D. (2012) The dormancy regulator DosR controls ribosome stability in hypoxic mycobacteria. *J. Biol. Chem.*, **287**, 24053–24063.
8. Sala,A., Bordes,P. and Genevaux,P. (2014) Multiple toxin-antitoxin systems in Mycobacterium tuberculosis. *Toxins (Basel)*, **6**, 1002–1020.
9. Javid,B., Sorrentino,F., Toosky,M., Zheng,W., Pinkham,J.T., Jain,N., Pan,M., Deighan,P. and Rubin,E.J. (2014) Mycobacterial mistranslation is necessary and sufficient for rifampicin phenotypic resistance. *Proc. Natl. Acad. Sci. U.S.A.*, **111**, 1132–1137.
10. Shell,S.S., Wang,J., Lapierre,P., Mir,M., Chase,M.R., Pyle,M.M., Gawande,R., Ahmad,R., Sarracino,D.A., Ioerger,T.R. *et al.* (2015) Leaderless transcripts and small proteins are common features of the mycobacterial translational landscape. *PLoS Genet.*, **11**, e1005641.
11. Wilson,D.N. (2014) Ribosome-targeting antibiotics and mechanisms of bacterial resistance. *Nat. Rev. Microbiol.*, **12**, 35–48.
12. Cannone,J.J., Subramanian,S., Schnare,M.N., Collett,J.R., D'Souza,L.M., Du,Y., Feng,B., Lin,N., Madabusi,L.V., Muller,K.M. *et al.* (2002) The comparative RNA web (CRW) site: an online database of comparative sequence and structure information for ribosomal, intron, and other RNAs. *BMC Bioinformatics*, **3**, 2.
13. Ramesh,M. and Woolford,J.L. Jr (2016) Eukaryote-specific rRNA expansion segments function in ribosome biogenesis. *RNA*, **22**, 1153–1162.
14. Gomez Ramos,L.M., Smeekens,J.M., Kovacs,N.A., Bowman,J.C., Wartell,R.M., Wu,R. and Williams,L.D. (2016) Yeast rRNA expansion segments: folding and function. *J. Mol. Biol.*, **428**, 4048–4059.
15. Wimberly,B.T., Brodersen,D.E., Clemons,W.M. Jr, Morgan-Warren,R.J., Carter,A.P., Vonrhein,C., Hartsch,T. and Ramakrishnan,V. (2000) Structure of the 30S ribosomal subunit. *Nature*, **407**, 327–339.
16. Fischer,N., Neumann,P., Konevega,A.L., Bock,L.V., Ficner,R., Rodnina,M.V. and Stark,H. (2015) Structure of the E. coli ribosome-EF-Tu complex at <3 A resolution by Cs-corrected cryo-EM. *Nature*, **520**, 567–570.
17. Sohmen,D., Chiba,S., Shimokawa-Chiba,N., Innis,C.A., Berninghausen,O., Beckmann,R., Ito,K. and Wilson,D.N. (2015) Structure of the Bacillus subtilis 70S ribosome reveals the basis for species-specific stalling. *Nat. Commun.*, **6**, 6941.
18. Eyal,Z., Matzov,D., Krupkin,M., Wekselman,I., Paukner,S., Zimmerman,E., Rozenberg,H., Bashan,A. and Yonath,A. (2015) Structural insights into species-specific features of the ribosome from

the pathogen Staphylococcus aureus. *Proc. Natl. Acad. Sci. U.S.A.*, **112**, E5805–E5814.
19. Cook,G.M., Berney,M., Gebhard,S., Heinemann,M., Cox,R.A., Danilchanka,O. and Niederweis,M. (2009) Physiology of mycobacteria. *Adv. Microb. Physiol.*, **55**, 81–182.
20. Li,X., Sun,Q., Jiang,C., Yang,K., Hung,L.W., Zhang,J. and Sacchettini,J.C. (2015) Structure of ribosomal silencing factor bound to mycobacterium tuberculosis ribosome. *Structure*, **23**, 1858–1865.
21. Grant,T. and Grigorieff,N. (2015) Measuring the optimal exposure for single particle cryo-EM using a 2.6 A reconstruction of rotavirus VP6. *Elife*, **4**, e06980.
22. Rohou,A. and Grigorieff,N. (2015) CTFFIND4: fast and accurate defocus estimation from electron micrographs. *J. Struct. Biol.*, **192**, 216–221.
23. Tang,G., Peng,L., Baldwin,P.R., Mann,D.S., Jiang,W., Rees,I. and Ludtke,S.J. (2007) EMAN2: an extensible image processing suite for electron microscopy. *J. Struct. Biol.*, **157**, 38–46.
24. Bai,X.C., Rajendra,E., Yang,G., Shi,Y. and Scheres,S.H. (2015) Sampling the conformational space of the catalytic subunit of human gamma-secretase. *Elife*, **4**, e11182.
25. Scheres,S.H. (2014) Beam-induced motion correction for sub-megadalton cryo-EM particles. *Elife*, **3**, e03665.
26. Scheres,S.H. and Chen,S. (2012) Prevention of overfitting in cryo-EM structure determination. *Nat. Methods*, **9**, 853–854.
27. Heymann,J.B. and Belnap,D.M. (2007) Bsoft: image processing and molecular modeling for electron microscopy. *J. Struct. Biol.*, **157**, 3–18.
28. Rother,M., Rother,K., Puton,T. and Bujnicki,J.M. (2011) ModeRNA: a tool for comparative modeling of RNA 3D structure. *Nucleic Acids Res.*, **39**, 4007–4022.
29. Jossinet,F. and Westhof,E. (2005) Sequence to Structure (S2S): display, manipulate and interconnect RNA data from sequence to structure. *Bioinformatics*, **21**, 3320–3321.
30. Trabuco,L.G., Villa,E., Mitra,K., Frank,J. and Schulten,K. (2008) Flexible fitting of atomic structures into electron microscopy maps using molecular dynamics. *Structure*, **16**, 673–683.
31. Adams,P.D., Afonine,P.V., Bunkoczi,G., Chen,V.B., Davis,I.W., Echols,N., Headd,J.J., Hung,L.W., Kapral,G.J., Grosse-Kunstleve,R.W. *et al.* (2010) PHENIX: a comprehensive Python-based system for macromolecular structure solution. *Acta Crystallogr. D Biol. Crystallogr.*, **66**, 213–221.
32. Chou,F.C., Sripakdeevong,P., Dibrov,S.M., Hermann,T. and Das,R. (2013) Correcting pervasive errors in RNA crystallography through enumerative structure prediction. *Nat. Methods*, **10**, 74–76.
33. Eswar,N., Webb,B., Marti-Renom,M.A., Madhusudhan,M.S., Eramian,D., Shen,M.Y., Pieper,U. and Sali,A. (2007) Comparative protein structure modeling using MODELLER. *Curr. Protoc. Protein Sci.*, doi:10.1002/0471250953.bi0506s15.
34. DiMaio,F., Song,Y., Li,X., Brunner,M.J., Xu,C., Conticello,V., Egelman,E., Marlovits,T.C., Cheng,Y. and Baker,D. (2015) Atomic-accuracy models from 4.5-A cryo-electron microscopy data with density-guided iterative local refinement. *Nat. Methods*, **12**, 361–365.
35. Emsley,P. and Cowtan,K. (2004) Coot: model-building tools for molecular graphics. *Acta Crystallogr. D Biol. Crystallogr.*, **60**, 2126–2132.
36. Zhang,J., Minary,P. and Levitt,M. (2012) Multiscale natural moves refine macromolecules using single-particle electron microscopy projection images. *Proc. Natl. Acad. Sci. U.S.A.*, **109**, 9845–9850.
37. Chen,V.B., Arendall,W.B. 3rd, Headd,J.J., Keedy,D.A., Immormino,R.M., Kapral,G.J., Murray,L.W., Richardson,J.S. and Richardson,D.C. (2010) MolProbity: all-atom structure validation for macromolecular crystallography. *Acta Crystallogr. D Biol. Crystallogr.*, **66**, 12–21.
38. Sim,A.Y., Levitt,M. and Minary,P. (2012) Modeling and design by hierarchical natural moves. *Proc. Natl. Acad. Sci. U.S.A.*, **109**, 2890–2895.
39. Grant,B.J., Rodrigues,A.P., ElSawy,K.M., McCammon,J.A. and Caves,L.S. (2006) Bio3d: an R package for the comparative analysis of protein structures. *Bioinformatics*, **22**, 2695–2696.
40. Pettersen,E.F., Goddard,T.D., Huang,C.C., Couch,G.S., Greenblatt,D.M., Meng,E.C. and Ferrin,T.E. (2004) UCSF Chimera—a visualization system for exploratory research and analysis. *J. Comput. Chem.*, **25**, 1605–1612.
41. Ivanov,A.V., Malygin,A.A. and Karpova,G.G. (2013) [Mg2+ ions affect the structure of the central domain of the 18S rRNA in the vicinity of the ribosomal protein S13 binding site]. *Mol. Biol. (Mosk)*, **47**, 157–166.
42. Liu,Q. and Fredrick,K. (2016) Intersubunit bridges of the bacterial ribosome. *J. Mol. Biol.*, **428**, 2146–2164.
43. Sprink,T., Ramrath,D.J., Yamamoto,H., Yamamoto,K., Loerke,J., Ismer,J., Hildebrand,P.W., Scheerer,P., Burger,J., Mielke,T. *et al.* (2016) Structures of ribosome-bound initiation factor 2 reveal the mechanism of subunit association. *Sci. Adv.*, **2**, e1501502.
44. Adamski,F.M., Atkins,J.F. and Gesteland,R.F. (1996) Ribosomal protein L9 interactions with 23 S rRNA: the use of a translational bypass assay to study the effect of amino acid substitutions. *J. Mol. Biol.*, **261**, 357–371.
45. Naganathan,A., Wood,M.P. and Moore,S.D. (2015) The large ribosomal subunit protein L9 enables the growth of EF-P deficient cells and enhances small subunit maturation. *PLoS One*, **10**, e0120060.
46. Leontis,N.B. and Westhof,E. (1998) A common motif organizes the structure of multi-helix loops in 16 S and 23 S ribosomal RNAs. *J. Mol. Biol.*, **283**, 571–583.
47. Correll,C.C., Beneken,J., Plantinga,M.J., Lubbers,M. and Chan,Y.L. (2003) The common and the distinctive features of the bulged-G motif based on a 1.04 A resolution RNA structure. *Nucleic Acids Res.*, **31**, 6806–6818.
48. Moore,P.B. (1999) Structural motifs in RNA. *Annu. Rev. Biochem.*, **68**, 287–300.
49. Ulyanov,N.B., Mujeeb,A., Du,Z., Tonelli,M., Parslow,T.G. and James,T.L. (2006) NMR structure of the full-length linear dimer of stem-loop-1 RNA in the HIV-1 dimer initiation site. *J. Biol. Chem.*, **281**, 16168–16177.
50. Ackerman,E.J., Saxena,S.K. and Ulbrich,N. (1988) Alpha-sarcin causes a specific cut in 28 S rRNA when microinjected into Xenopus oocytes. *J. Biol. Chem.*, **263**, 17076–17083.
51. Endo,Y. and Tsurugi,K. (1988) The RNA N-glycosidase activity of ricin A-chain. The characteristics of the enzymatic activity of ricin A-chain with ribosomes and with rRNA. *J. Biol. Chem.*, **263**, 8735–8739.
52. Tesh,V.L. and O'Brien,A.D. (1991) The pathogenic mechanisms of Shiga toxin and the Shiga-like toxins. *Mol. Microbiol.*, **5**, 1817–1822.
53. Winther,K.S., Brodersen,D.E., Brown,A.K. and Gerdes,K. (2013) VapC20 of Mycobacterium tuberculosis cleaves the sarcin-ricin loop of 23S rRNA. *Nat. Commun.*, **4**, 2796.
54. Szewczak,A.A., Moore,P.B., Chang,Y.L. and Wool,I.G. (1993) The conformation of the sarcin/ricin loop from 28S ribosomal RNA. *Proc. Natl. Acad. Sci. U.S.A.*, **90**, 9581–9585.
55. Dashti,A., Schwander,P., Langlois,R., Fung,R., Li,W., Hosseinizadeh,A., Liao,H.Y., Pallesen,J., Sharma,G., Stupina,V.A. *et al.* (2014) Trajectories of the ribosome as a Brownian nanomachine. *Proc. Natl. Acad. Sci. U.S.A.*, **111**, 17492–17497.
56. Mohan,S. and Noller,H.F. (2017) Recurring RNA structural motifs underlie the mechanics of L1 stalk movement. *Nat. Commun.*, **8**, 14285.
57. Li,G.W., Oh,E. and Weissman,J.S. (2012) The anti-Shine-Dalgarno sequence drives translational pausing and codon choice in bacteria. *Nature*, **484**, 538–541.
58. Beckmann,R., Spahn,C.M., Eswar,N., Helmers,J., Penczek,P.A., Sali,A., Frank,J. and Blobel,G. (2001) Architecture of the protein-conducting channel associated with the translating 80S ribosome. *Cell*, **107**, 361–372.
59. Sweeney,R., Chen,L. and Yao,M.C. (1994) An rRNA variable region has an evolutionarily conserved essential role despite sequence divergence. *Mol. Cell. Biol.*, **14**, 4203–4215.
60. Stanley,R.E., Blaha,G., Grodzicki,R.L., Strickler,M.D. and Steitz,T.A. (2010) The structures of the anti-tuberculosis antibiotics viomycin and capreomycin bound to the 70S ribosome. *Nat. Struct. Mol. Biol.*, **17**, 289–293.
61. Ippolito,J.A., Kanyo,Z.F., Wang,D., Franceschi,F.J., Moore,P.B., Steitz,T.A. and Duffy,E.M. (2008) Crystal structure of the oxazolidinone antibiotic linezolid bound to the 50S ribosomal subunit. *J. Med. Chem.*, **51**, 3353–3356.
62. Wilson,D.N., Schluenzen,F., Harms,J.M., Starosta,A.L., Connell,S.R. and Fucini,P. (2008) The oxazolidinone antibiotics

perturb the ribosomal peptidyl-transferase center and effect tRNA positioning. *Proc. Natl. Acad. Sci. U.S.A.*, **105**, 13339–13344.
63. Barnhill,A.E., Brewer,M.T. and Carlson,S.A. (2012) Adverse effects of antimicrobials via predictable or idiosyncratic inhibition of host mitochondrial components. *Antimicrob. Agents Chemother.*, **56**, 4046–4051.
64. Pacheu-Grau,D., Gomez-Duran,A., Iglesias,E., Lopez-Gallardo,E., Montoya,J. and Ruiz-Pesini,E. (2013) Mitochondrial antibiograms in personalized medicine. *Hum. Mol. Genet.*, **22**, 1132–1139.
65. Amunts,A., Brown,A., Toots,J., Scheres,S.H. and Ramakrishnan,V. (2015) Ribosome. The structure of the human mitochondrial ribosome. *Science*, **348**, 95–98.
66. Ben-Shem,A., Garreau de Loubresse,N., Melnikov,S., Jenner,L., Yusupova,G. and Yusupov,M. (2011) The structure of the eukaryotic ribosome at 3.0 A resolution. *Science*, **334**, 1524–1529.
67. Schluenzen,F., Tocilj,A., Zarivach,R., Harms,J., Gluehmann,M., Janell,D., Bashan,A., Bartels,H., Agmon,I., Franceschi,F. *et al.* (2000) Structure of functionally activated small ribosomal subunit at 3.3 angstroms resolution. *Cell*, **102**, 615–623.
68. Wilson,D.N. and Doudna Cate,J.H. (2012) The structure and function of the eukaryotic ribosome. *Cold Spring Harb. Perspect. Biol.*, **4**, a011536.
69. Desai,N., Brown,A., Amunts,A. and Ramakrishnan,V. (2017) The structure of the yeast mitochondrial ribosome. *Science*, **355**, 528–531.
70. Khatter,H., Myasnikov,A.G., Natchiar,S.K. and Klaholz,B.P. (2015) Structure of the human 80S ribosome. *Nature*, **520**, 640–645.
71. Dinman,J.D. (2005) 5S rRNA: structure and function from head to toe. *Int. J. Biomed. Sci.*, **1**, 2–7.
72. Bieri,P., Leibundgut,M., Saurer,M., Boehringer,D. and Ban,N. (2017) The complete structure of the chloroplast 70S ribosome in complex with translation factor pY. *EMBO J.*, **36**, 475–486.
73. Ahmed,T., Yin,Z. and Bhushan,S. (2016) Cryo-EM structure of the large subunit of the spinach chloroplast ribosome. *Sci. Rep.*, **6**, 35793.
74. Graf,M., Arenz,S., Huter,P., Donhofer,A., Novacek,J. and Wilson,D.N. (2016) Cryo-EM structure of the spinach chloroplast ribosome reveals the location of plastid-specific ribosomal proteins and extensions. *Nucleic Acids Res.*, **45**, 2887–2896.
75. Hentschel,J., Burnside,C., Mignot,I., Leibundgut,M., Boehringer,D. and Ban,N. (2017) The complete structure of the mycobacterium smegmatis 70S ribosome. *Cell Rep.*, **20**, 149–160.